ACS Energy LETTERS

pubs.acs.org/journal/aelccp

Letter

Disentangling the Electro-Ionic Interplay in Perovskite LED Degradation via Operando Modulated Spectroscopies

Rafael S. Sánchez,* Alexis Villanueva-Antolí, Sarika Kumari, Anna M. Kotowska, Matthew Piggott, David J. Scurr, Luis Lanzetta, Francisco Fabregat-Santiago, and Iván Mora-Seró

Cite This: https://doi.org/10.1021/acsenergylett.6c01829

Read Online

ACCESS | Metrics & More | Article Recommendations | Supporting Information

ABSTRACT: Colloidal perovskite nanocrystal light-emitting diodes (PeLEDs) currently achieve near-theoretical efficiencies; however, their operational stability remains fundamentally constrained by complex electro-ionic interactions. Conventional characterization techniques fail to decouple electronic charge dynamics from ionic mechanisms. Here, we utilize operando impedance spectroscopy (IS) and voltage-modulated electroluminescence (VMEL) to disentangle these phenomena in efficient $CsPbBr_3$ PeLEDs. We isolate a characteristic intermediate-frequency (~5 kHz) inductive-like VMEL signature directly correlated with the non-monotonic luminance evolution of the devices. By extracting an activation energy of 0.29 ± 0.03 eV (matching bulk bromide migration energetics) and demonstrating quantitative agreement with ion-screening models, we unambiguously trace this signature to the electric-field-induced desorption of surface ligands. This progressive ligand loss generates halide vacancies that drift into the bulk, irrevocably quenching emission. Ultimately, this approach provides a universal diagnostic framework to assess electro-ionic coupling, guiding targeted surface passivation to unlock the long-term stability of emerging optoelectronics.

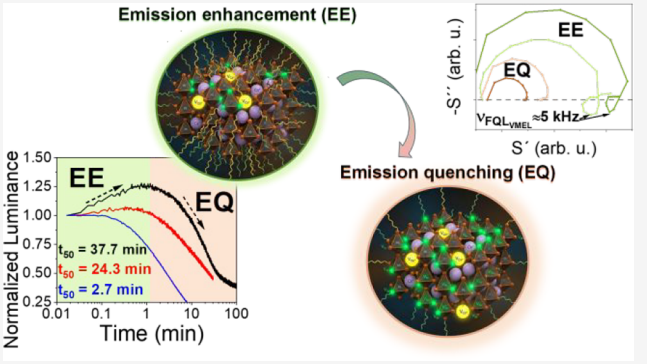

Halide perovskites are leading semiconductors for next-generation displays due to their tunable narrow-band emission, defect tolerance, and near-unity photoluminescence quantum yields (PLQYs).[1,2] However, bulk 3D films often exhibit a low exciton binding energy (E_b ≈ 30–50 meV) due to their high relative dielectric constant (ε_r),[3,4] rendering radiative recombination an inefficient bimolecular process. To overcome this, dimensional reduction (e.g., bulk 2D or quasi-2D structures) and the spatial confinement of perovskite nanocrystals (PeNCs) have been extensively explored to enhance E_b and boost excitonic recombination.[5−10] While the external quantum efficiencies (EQEs) of bulk-like and PeNC-based light-emitting diodes (PeLEDs) now approach theoretical limits,[5,11−14] long-term operational stability remains a critical bottleneck. Notably, the operational half-lifetime (t_{50}) of PeNC PeLEDs spans from seconds to a few hundred minutes, significantly shorter than the thousands of hours achieved by bulk devices.[14−17] Unfortunately, the exact origins of this limited reliability remain poorly understood, making stability improvements a major challenge. Although the synthesis of PeNCs yields high-quality emitters, using surfactants to control particle size, prevent aggregation, and passivate surface defects introduces severe operational vulnerabilities.[18,19] Specifically, capping agents, such as oleic acid (OA) and oleylamine (OLA), which bind to the PeNCs by partially replacing native surface ions, are highly labile.[20,21] This lability contributes to the generation of surface defects and the premature degradation of the semiconductor. Ultimately, the limited performance reliability arises from the complex electro-ionic nature of perovskites, where the interplay between applied electric fields, interfaces, and ionic migration dynamically alters the electro-optical properties of the devices. Disentangling these concurrent phenomena requires advanced operando electro-optical techniques.[22,23]

In this context, frequency-domain techniques, such as impedance spectroscopy (IS) and voltage-modulated electroluminescence (VMEL), are particularly well-suited to dissect these processes, as each phenomenon manifests in distinct frequency regimes according to its characteristic time constant. Indeed, we previously demonstrated the suitability of IS and VMEL for the study of highly efficient PeLEDs.[24] The broad capacitive behavior (from 100 kHz to 100 Hz) in the impedance spectrum corresponds to the accumulation of charge and subsequent filling

Received: June 23, 2026
Revised: July 31, 2026
Accepted: August 7, 2026

of electronic states at the interfaces prior to effective charge injection into the emissive layer, whereas the main VMEL capacitive response (100–10 kHz) correlates with the modulation of luminous intensity. Crucially, we identified two additional positive reactances: a low-frequency inductive feature detected via IS (IF_{IS} at ∼20 Hz) mainly associated with the delayed charge recombination and an intermediate-frequency fourth-quadrant loop detected via VMEL (FQL_{VMEL} at ∼5 kHz) that stems from a delayed modulation of the photon emission (see Note S1 and Figure S1). While previous studies on perovskite solar cells (PSCs) have associated IS inductances with dephased charge recombination driven by ionic accumulation[25] or bulk recombination,[26−28] the precise physical origin of the FQL_{VMEL} in PeLEDs and its implications for device degradation remain elusive.

Here, we exploit VMEL spectroscopy as an operando probe to elucidate the mechanisms driving the premature degradation of highly efficient $CsPbBr_3$ PeLEDs and their connection to the intermediate-frequency positive reactance. We demonstrate that the FQL_{VMEL} signature is directly correlated with the non-monotonic performance evolution of the devices. By extracting the activation energy (E_a) of this operational dynamic, we trace the degradation pathway to the electric-field-induced desorption of OA/OLA ligands and the subsequent trap-assisted migration of halide vacancies. These findings establish a direct mechanistic link between macroscopic device failure and microscopic ligand dynamics, providing a quantitative framework to evaluate and design robust surface-passivation strategies for perovskite optoelectronics.

To establish a comprehensive understanding of the electro-optical dynamics in PeNC-based systems, we performed multi-scale characterization encompassing the fundamental properties of the $CsPbBr_3$ PeNCs and the operando performance of the resulting highly efficient PeLEDs. The devices were investigated through steady-state and transient time-domain measurements, complemented by frequency-domain spectroscopies (IS and VMEL) to decouple electronic and ionic contributions and decipher the degradation mechanisms that limit the long-term performance of these devices.

Optical and Morphological Properties of $CsPbBr_3$ PeNCs

The constituent PeNCs were synthesized via a hot-injection method and integrated into highly efficient device architectures following our previously optimized protocols (see theSupporting Information for further details).[12,24] The absorption and photoluminescence (PL) spectra of the purified $CsPbBr_3$ PeNCs in solution exhibit features that are in excellent agreement with those expected for this composition (Figure 1a).[29,30] Although the as-prepared PeNCs exhibit an initial photoluminescence quantum yield in solution ($PLQY_{sol}$) of ≈90%, device fabrication necessitates the removal of excess unreacted reagents and high-boiling point solvents. This mandatory purification induces a partial loss of surface capping agents, reducing the $PLQY_{sol}$ to 46.0 ± 6.8% (see Table S1). Nonetheless, the optical integrity of the emitters is largely preserved upon thin-film formation, yielding highly luminescent solid-state layers ($PLQY_{film}$ = 30.7 ± 1.1%) suitable for efficient PeLED integration. Morphological characterization via transmission electron microscopy (TEM) reveals that the purified PeNCs maintain a well-defined cubic geometry with an average edge length of ≈13 nm (Figures 1b and S2).

Electro-Optical Performance of $CsPbBr_3$ PeLEDs

The purified PeNCs were integrated into the device architecture depicted in Figure 1c. To ensure high statistical reliability, the electro-optical metrics were evaluated across a batch of 80 individual PeLEDs with an active area of 8 mm^2. The averaged current density–voltage–luminance (J–V–L) characteristics (Figure 1d) reveal a low turn-on voltage (V_{on}) of 3.2 V and an outstanding average maximum luminance (L_{max}) exceeding 4×10^4 $cd{\cdot}m^{-2}$. Furthermore, the devices exhibit state-of-the-art efficiency metrics, reaching average maximum external quantum efficiency (EQE_{max}) and current efficiency (CE_{max}) values of 20.0% and 61.3 $cd{\cdot}A^{-1}$, respectively (Figure 1e). Despite their high initial efficiencies, the devices exhibit bias-dependent operational instability. Figure 1f displays the luminance evolution over time under constant-current driving at 0.16, 1.65, and 24.63 $mA{\cdot}cm^{-2}$, yielding initial luminances (L_0) of 10^2, 10^3, and 10^4 $cd{\cdot}m^{-2}$, respectively. The corresponding operational half-lifetimes (t_{50}) are 37.7, 24.3, and 2.7 min, respectively, revealing that higher injection currents exponentially accelerate performance degradation (see Figure S3a). Notably, at lower L_0 regimes, the brightness evolution is distinctly non-monotonic: an initial emission enhancement (EE) stage during the first 1–2 min is followed by a gradual emission quenching (EQ) phase. The driving voltage traces closely mirror this unsteady behavior (Figure S3b).

To elucidate the microscopic origin of this degradation, we probed the active areas of fresh and electrically aged devices using steady-state photoluminescence (PL) spectroscopy. While the spectral distribution remains stable after aging (Figures 1g and S4), the absolute PL intensity drops significantly. The magnitude of this PL quenching correlates linearly with the total charge injected into the device (Figure S5). Furthermore, time-resolved PL (TRPL) measurements reveal a severe reduction in the average carrier lifetime (τ_{avg}) upon aging (Figure 1h and Table S2). Collectively, these optical signatures demonstrate that electrical stress drives the proliferation of non-radiative charge recombination pathways. However, standard steady-state and time-resolved optical techniques cannot definitively discriminate whether this trap generation occurs in the perovskite bulk or at the interfaces, necessitating the use of advanced operando modulated techniques.

Operando Frequency-Domain Spectroscopies and Degradation Signatures

To decouple the underlying instability mechanisms, we utilized small-perturbation IS and VMEL across three device architectures: PeLEDs, quantum dot LEDs (QLEDs), and organic LEDs (OLEDs), as detailed in Figures 1c and 2a, respectively. The IS Nyquist plots of the $CsPbBr_3$ PeLEDs under different DC biases reveal a noticeable low-frequency inductance (IF_{IS} ∼ 20 Hz) extending into the fourth quadrant (Figure 2b, left inset), ascribed to a delayed charge recombination modulated by ion accumulation at the transport layer interfaces.[28] Furthermore, the corresponding VMEL spectra isolate an additional fourth-quadrant phenomenon at intermediate frequencies (FQL_{VMEL} ∼ 5 kHz) stemming from a delayed photon emission within the perovskite bulk (Figure 2c).

To rigorously confirm that these fourth-quadrant features are intrinsic to the mixed electro-ionic nature of the perovskite rather than generic artifacts from the measurement setup, we evaluated CdSe/CdS/ZnS QLEDs as ion-free reference

https://doi.org/10.1021/acsenergylett.6c01829
ACS Energy Lett. XXXX, XXX, XXX−XXX

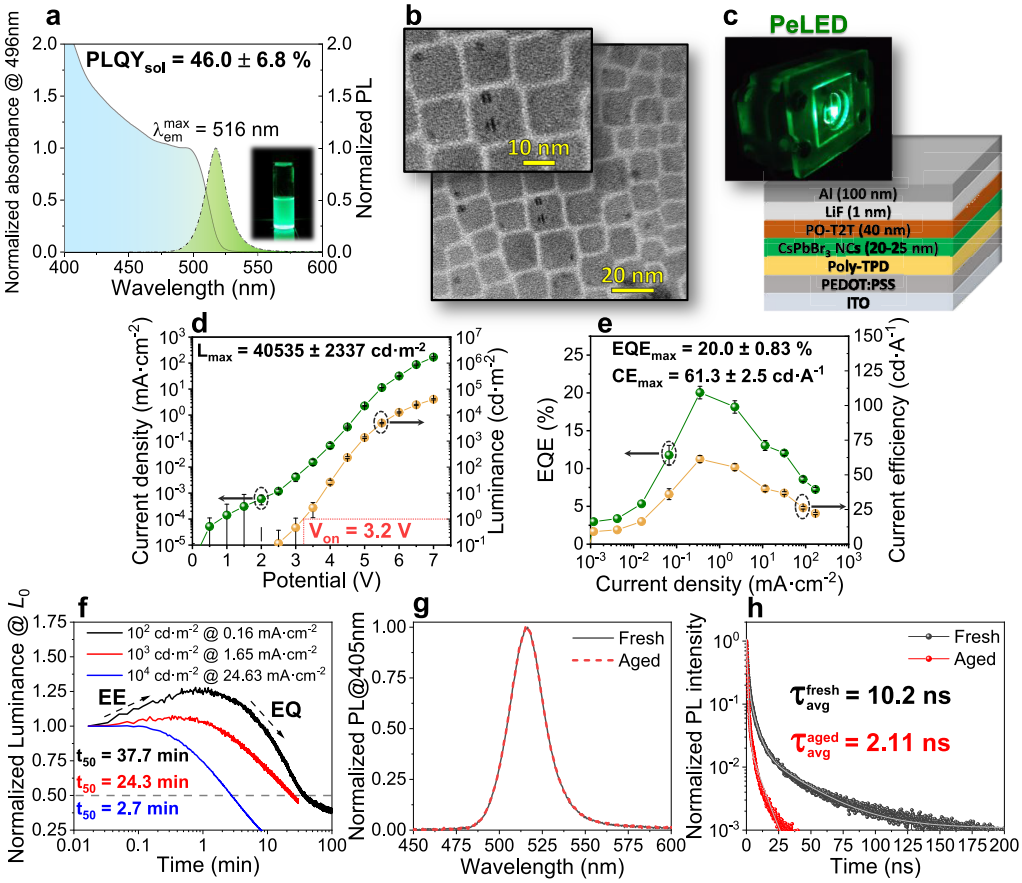

Figure 1. Optical and morphological characterization of $CsPbBr_3$NCs and performance of PeLEDs. (a) Normalized absorption and PL spectra of PeNCs in hexane. Samples were excited at λ_{exc} = 405 nm; the obtained $PLQY_{sol}$ and λ_{em}^{max} values are indicated. The inset shows a vial with PeNCs dispersed in hexane under UV light. (b) Transmission electron microscopy (TEM) image of the PeNCs, with the inset providing a higher-magnification view. (c) Photograph of an operating PeLED at 5.0 V and schematic of the device architecture. Layer thicknesses are estimated from our previous work.[12] (d) *J*–*V* and *L*–*V* curves averaged across 80 independent active areas (4 per device) with the corresponding standard deviation (SD). The turn-on voltage (V_{on}) was estimated at 1 cd·m^{-2} (red-dotted lines), and the maximum averaged luminance (L_{max}) obtained at 7 V (169.1 mA·cm^{-2}) is indicated. (e) EQE–*J* and CE–*J* curves averaged across 80 independent active areas with the corresponding SD. The averaged EQE_{max} and CE_{max} values registered at 0.35 mA·cm^{-2} are indicated. (f) Operational stability tracked at three different constant current densities (corresponding to distinct initial luminance levels, L_0). Dashed arrows delineate the EE and EQ regimes. The t_{50} values were estimated from the intersection of each curve with the horizontal light-gray dashed line. (g) Normalized in situ PL spectra of a PeLED active area before (solid black line) and after (red dashed line) electrical aging at 0.10 mA for 10 min. (h) TRPL (λ_{exc} = 405 nm) decays registered at the active area of a PeLED before (fresh) and after aging at 0.13 mA for 5 min. Solid gray lines represent the tri- and bi-exponential numerical fits for the fresh and aged devices, respectively.

nanocrystal-based devices. As expected, the control QLEDs exhibited strictly capacitive behavior, devoid of any positive reactance in both their IS and VMEL responses (Figure 2b right inset and Figure 2c). Moreover, to definitively rule out artifacts originating from the charge selective layers, we fabricated a control OLED employing an identical device architecture but substituting the PeNCs with an organic dye (C-153). The IS response of this OLED lacks any inductive feature, which confirms that the IF_{IS} at ∼20 Hz observed in the PeLEDs is unambiguously ascribed to the halide perovskite (Figure S6). While its VMEL spectrum exhibits a minor feature that marginally crosses into the fourth quadrant (Figure 2c inset, potentially within the noise margin), its distinctly lower characteristic frequency (∼25 Hz) unequivocally rules out a common physical origin with the FQL_{VMEL} of the PeLEDs observed at ∼5 kHz. Together with the QLED data, these results confirm that the low-frequency IS inductance and the intermediate-frequency VMEL fourth-quadrant loop are intrinsic spectroscopic signatures of the perovskite layer.

Having isolated these physical features, we tracked the temporal evolution of the VMEL spectra to elucidate the role of the FQL_{VMEL} in device degradation. Consecutive measurements (Figure 2d) reveal a distinct spectral progression tightly coupled to the non-monotonic luminance evolution. During the initial EE stage, the main capacitive semicircle expands, reflecting the increased emission intensity, while the FQL_{VMEL} remains clearly resolved despite a slight reduction in magnitude (1st and 2nd scans in Figure 2d, ∼1 min per scan). However, upon prolonged operation, as the device transitions into the EQ regime, the capacitive arc progressively shrinks, and the 5 kHz feature concurrently vanishes (3rd to 5th measurements in Figure 2d). This spectral evolution firmly establishes the FQL_{VMEL} as the direct operando footprint of the dynamic degradation mechanism governing the PeLED stability.

https://doi.org/10.1021/acsenergylett.6c01829
ACS Energy Lett. XXXX, XXX, XXX–XXX

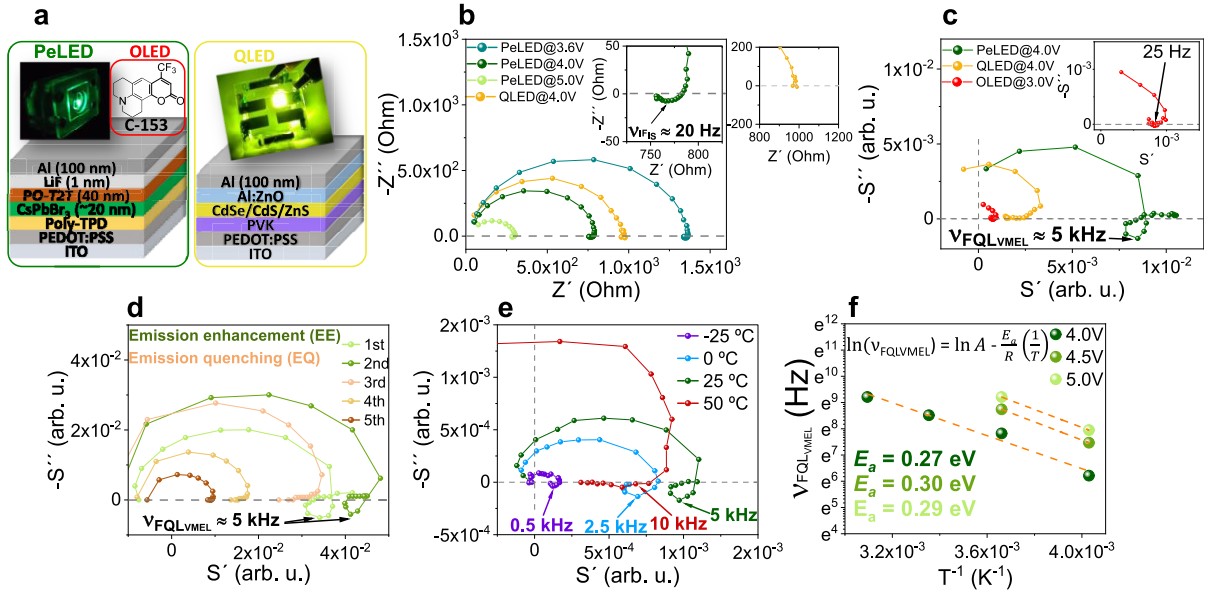

Figure 2. Frequency-domain operando spectroscopy and thermodynamic analysis. (a) Cross-sectional schematics and photographs of the PeLED, QLED, and OLED architectures employed for the advanced electro-optical characterization. (b) Impedance spectroscopy (IS) Nyquist plots for the $CsPbBr_3$ PeLEDs and CdSe/CdS/ZnS control QLEDs at various applied potentials. Insets (left and right) highlight the low-frequency region at 4.0 V, revealing the presence of an inductive loop (IF_{IS}) in the PeLEDs (green dots) and its strict absence in the ion-free QLEDs (yellow dots). The gray dashed lines delineate the different quadrants to highlight the entry into the fourth quadrant. (c) VMEL spectra of the PeLED, QLED, and control OLED at the indicated biases. The OLED spectrum (inset) is magnified for scale. The intermediate-frequency fourth-quadrant loop (FQL_{VMEL}) unique to the PeLEDs is indicated along with its characteristic $\nu_{FQLVMEL}$. (d) Consecutive operando VMEL spectra registered at 4.0 V on a PeLED, capturing the dynamic transition from the emission enhancement (EE, greenish curves) to the emission quenching (EQ, brownish curves) regime. (e) VMEL spectra of the PeLEDs registered at 4.0 V at different temperatures. The $\nu_{FQLVMEL}$ values at each temperature are indicated. (f) Arrhenius plots of ln ($\nu_{FQLVMEL}$) versus inverse temperature at different potentials. Orange dashed lines represent the linear fits used to extract the associated activation energies (E_a). Data were collected across 6 independent active pixels from 2 separate fabrication batches (3 pixels from batch 1 for –25, 0 and +25 °C at 4.0, 4.5, and 5.0 V, respectively, and 3 pixels from batch 2 for +50 °C, with 1 pixel per voltage).

Electro-Ionic Interplay and Degradation Mechanism

Having linked the intermediate-frequency FQL_{VMEL} to the dynamic EE/EQ regimes, we performed temperature-dependent VMEL measurements to extract the thermodynamic parameters governing this response. The VMEL spectra registered at 4.0 V for temperatures ranging from -25 to +50 °C are shown in Figure 2e (see Figure S7 for the raw VMEL spectra acquired at other potentials and temperatures). Tracking the characteristic frequency of the FQL_{VMEL} ($\nu_{FQLVMEL}$) across varying temperatures and DC voltages reveals an excellent linear correlation when represented in an Arrhenius plot (Figure 2f). The E_a extracted from the slope of these linear fits is remarkably independent of the DC bias (see Figure S8 for the fitting details). Averaging across the tested potentials yields a single characteristic E_a^{avg} of 0.29 ± 0.03 eV (Figure S9). Notably, at higher voltages (4.5 and 5.0 V) and elevated temperatures (25 and 50 °C), the rapid onset of the EQ regime outpaces the measurement timescale, precluding the observation of the FQL_{VMEL}.

To contextualize this activation barrier within the reported ionic mobility of halide perovskites,[31] we compared our findings with established values for halide exchange. While solution-phase measurements of $CsPbBr_3$ PeNCs yield variable activation barriers depending on the ion exchange mechanism (e.g., ≈0.33 eV[32] for single ligand detachment versus ≈0.63 eV[33] for ligand-mediated inter-nanocrystal exchange), our operando solid-state measurements strictly align with bulk halide migration. Specifically, our extracted E_a^{avg} of 0.29 eV is in excellent quantitative agreement with the activation energies reported for bromide migration in solid-state $CsPbBr_3$ electrodes (0.25 eV),[34] $MAPbBr_3$ solar cells (0.25 eV),[35] and bulk-nanocrystal heterojunctions (≈0.32 eV).[36] Consequently, we unambiguously assign the FQL_{VMEL} signature to halide migration phenomena triggered by the operational electric field. Physically, the FQL_{VMEL} footprint corresponds to a phase-delayed radiative recombination of charge carriers modulated by the ionic redistribution. The exact origin of this delay can be understood through the theoretical framework proposed by Clarke et al.[28]; in ultra-thin perovskite layers (~20 nm, roughly two PeNC monolayers)[12] operating under high carrier injection, mobile ions are slightly displaced, creating a localized population of "excess ions" that neutralize small electronic charges. Theoretically, this dynamic screening occurs over timescales roughly 200 times faster than bulk ion migration.[28] Strikingly, in our operando measurements, the frequency ratio of the observed positive reactances ($\nu_{FQLVMEL}/\nu_{IFIS}$) was estimated to be on the order of ~250, demonstrating a strong agreement in order of magnitude with Clarke's theoretical predictions. At medium frequencies (~5 kHz), these excess ions can only partially respond to the electronic charge, resulting in an ion-modulated recombination rate that directly produces the phase delay observed in the VMEL spectra. Ultimately, this profound local disorder drives the premature loss of the emissive properties of the PeNCs, as evidenced by the EQ regime (Figure 1f) and the PL quenching confined to the PeLED active area

https://doi.org/10.1021/acsenergylett.6c01829
ACS Energy Lett. XXXX, XXX, XXX–XXX

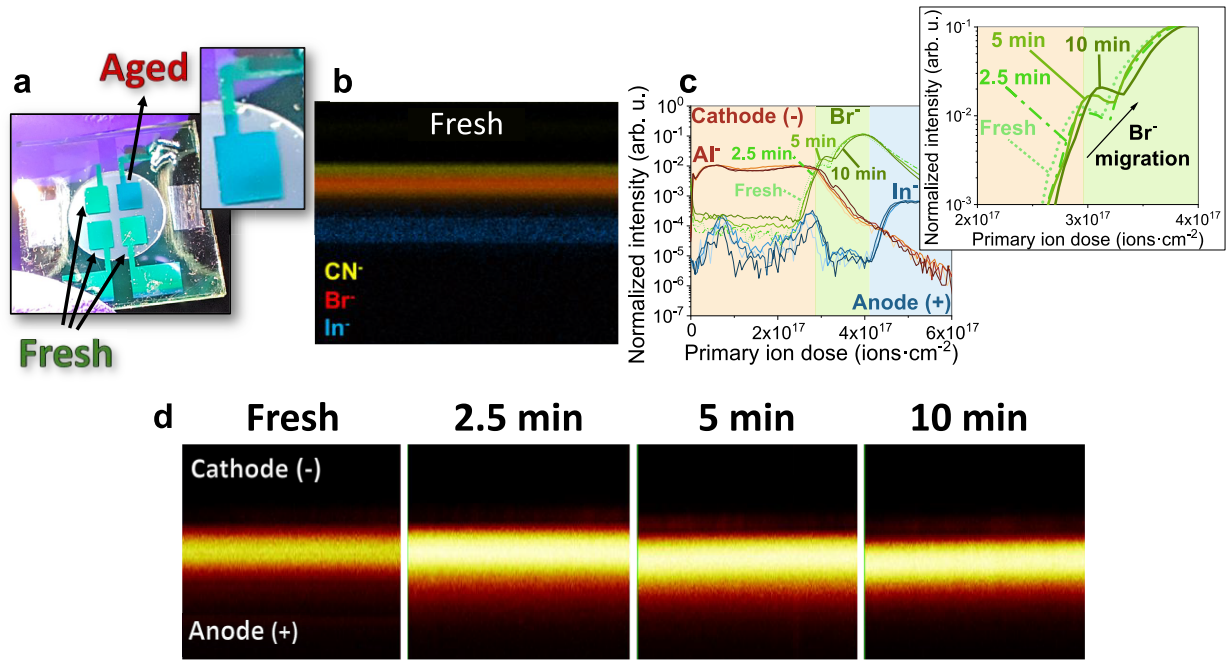

Figure 3. Direct visualization of field-induced degradation in PeLEDs. (a) Photograph of a PeLED substrate under white light illumination, containing three fresh active areas and one electrically aged pixel (5.0 V for 10 min). The inset demonstrates that the PL quenching is strictly confined to the electrically stressed active area. (b) Compositional ToF-SIMS depth profile of a fresh device. Secondary ions for In^-, Br^-, and CN^- serve as key elemental and molecular fragment markers for the ITO, perovskite, and PO-T2T layers, respectively, confirming a highly conformal stacked architecture. (c) Evolution of the Al^- (brown), Br^- (green), and In^- (blue) depth profile traces for PeLEDs at different aging states (fresh versus aged for 2.5, 5, and 10 min at 5.0 V), revealing a progressive accumulation of halides toward the anode interface (right). Darker color shades correspond to longer aging times. The inset shows a magnification of the Br^- ion intensity, highlighting the field-driven halide drift. (d) Corresponding 2D ToF-SIMS cross-sectional maps (xz data segments) of the Br^- distribution at the respective aging stages. The physical positions of the cathode (top) and anode (bottom) interfaces are indicated.

(Figure 3a). To definitively corroborate the macroscopic halide migration inferred from the VMEL thermodynamics, we performed depth-profiling time-of-flight secondary ion mass spectrometry (ToF-SIMS) on PeLEDs at different stages of operational aging (fresh versus aged at 5.0 V for 2.5, 5, and 10 min).

Compositional ToF-SIMS analysis tracks In^-, SO_3^-, Br^-, CN^-, and Al^- as key elemental markers for the ITO, PEDOT:PSS, PeNCs, PO-T2T, and Al layers, respectively, confirming a highly conformal stacked morphology (Figures 3b and S10, S11). Under continuous forward bias, the normalized depth profiles (Figure 3c) reveal a progressive spatial drift of Br^- ions from the perovskite layer toward the anode, directly demonstrating electric-field-induced halide migration. This is corroborated by 2D cross-sectional images (Figure 3d), which show an intensified Br^- front stemming from the escalating lattice disorder under electrical stress. Interestingly, the CN^- profile, which serves as a characteristic ToF-SIMS secondary fragment tracking C−N containing organic species, such as oleylammonium (OLA^+) ligands and PO-T2T, exhibits an aging drift parallel to Br^- (Figure S10). This indicates that perovskite lattice rearrangement dynamically disrupts the adjacent organic interface. Note that the CN^- depth profile overlaps with Br^- even in fresh devices (Figure S11), a feature reflecting the potential partial interpenetration of the thermally evaporated PO-T2T layer into the perovskite surface alongside the presence of OLA^+ ligands, both of which yield CN^- fragments during ion-beam sputtering. Crucially, the static In^- profile (Figure S10) rules out macroscopic thermal intermixing, isolating halide migration as a purely electrostatically driven process. Based on these insights, we propose a holistic degradation mechanism (Figure 4).

Under bias, the ionic A−X and metavalent B−X bonds weaken,[37,38] prompting the field-induced desorption of oleylammonium (OLA^+) and oleate (OA^-) surface ligands. Initially, partial ligand loss reduces steric hindrance for charge injection, temporarily boosting luminance (EE regime). However, prolonged electrical stress drives excessive OA^- desorption, generating surface bromide vacancies (V_{Br}). Concurrently, OLA^+ desorption yields cesium vacancies (V_{Cs}), with the simultaneous withdrawal of Br^- ions (or oleates) to preserve charge neutrality, thereby further amplifying the V_{Br} generation. These vacancies propagate into the bulk via halide hopping[39] or inter-nanocrystal pathways,[33] establishing a dynamic chemisorption/desorption equilibrium that accelerates ion migration. Ultimately, this severe electrochemically driven rearrangement creates non-radiative trap states that irrevocably quench device emission (EQ regime).

In summary, we have established a powerful methodology to definitively decouple purely electrical processes from delayed ionic phenomena in perovskite LEDs by combining operando impedance spectroscopy (IS) and voltage-modulated electroluminescence (VMEL). Isolating the intermediate-frequency VMEL signature (FQL_{VMEL}) allows for the first direct thermodynamic quantification of field-induced degradation under actual device operation, yielding an activation barrier of 0.29 ± 0.03 eV. This explicitly links macroscopic brightness evolution to microscopic ligand desorption and subsequent

https://doi.org/10.1021/acsenergylett.6c01829
ACS Energy Lett. XXXX, XXX, XXX−XXX

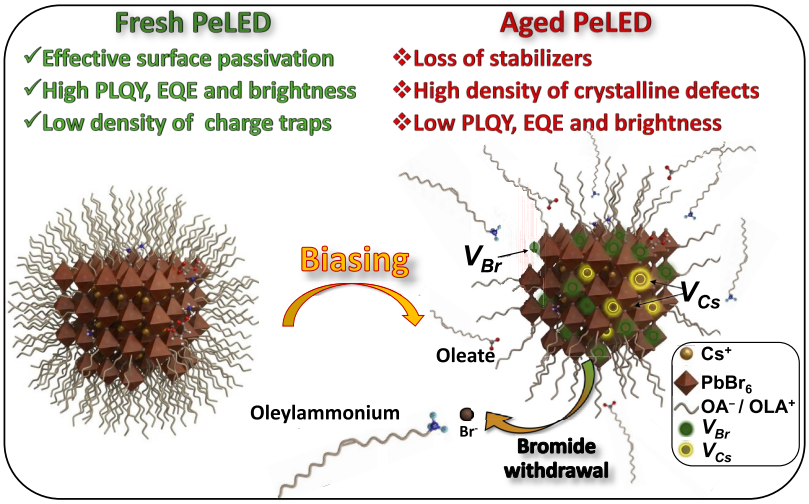

Figure 4. Mechanistic model of field-induced degradation in PeLEDs. Schematic illustration of the PeNC surface evolution before and after prolonged electrical biasing. The electric field drives the continuous desorption of surface stabilizing ligands, promoting the formation of vacancies that exacerbate halide migration within the perovskite bulk. The dynamic hopping of Br^- ions facilitates the occupation and subsequent inward migration of surface bromide vacancies (V_{Br}), inducing a severe ionic rearrangement and lattice disorder. Simultaneously, the loss of alkylammonium ligands induces the formation of cesium vacancies (V_{Cs}) and necessitates the concurrent withdrawal of Br^- ions (or oleates) to preserve local charge neutrality, thereby indirectly amplifying the V_{Br} generation.

halide migration. Beyond explaining $CsPbBr_3$ device failure, this approach provides a versatile diagnostic framework to assess electro-ionic coupling in PeLEDs, setting a promising foundation to test its potential universality across broader perovskite compositions and other mixed-conductor optoelectronics. Understanding the main degradation mechanism provides clear guidelines for engineering robust ligand chemistries capable of suppressing field-induced desorption at the nanocrystal interface.

■ ASSOCIATED CONTENT

Supporting Information

The Supporting Information is available free of charge at https://pubs.acs.org/doi/10.1021/acsenergylett.6c01829.

Materials, fabrication procedures, and characterization methods; physical interpretation of the anomalous positive reactance (Note S1); time-domain analysis of modulated signals (Figure S1); particle size distribution histograms (Figure S2); evolution of electro-optical characteristics under operational conditions (Figure S3); comparison of EL and PL spectra (Figure S4); normalized PL intensity evolution upon aging (Figure S5); IS spectrum of an OLED (Figure S6); VMEL spectra at different temperatures and potentials (Figure S7); Arrhenius plots and activation energies extracted from VMEL (Figures S8 and S9); ToF-SIMS depth and 3D compositional profiles at different aging states (Figures S10 and S11); and optical properties of $CsPbBr_3$ PeNCs and PL decay fitting parameters (Tables S1 and S2) (DOCX)

■ AUTHOR INFORMATION

Corresponding Author

Rafael S. Sánchez – *Institute of Advanced Materials (INAM), Universitat Jaume I, Castelló 12006, Spain;* orcid.org/0000-0001-8948-6120; Email: rasanche@uji.es

Authors

Alexis Villanueva-Antolí – *Institute of Advanced Materials (INAM), Universitat Jaume I, Castelló 12006, Spain*

Sarika Kumari – *Institute of Advanced Materials (INAM), Universitat Jaume I, Castelló 12006, Spain*

Anna M. Kotowska – *Advanced Materials and Healthcare Technologies, School of Pharmacy, University of Nottingham, Nottingham NG7 2RD, U.K.*

Matthew Piggott – *Advanced Materials and Healthcare Technologies, School of Pharmacy, University of Nottingham, Nottingham NG7 2RD, U.K.*

David J. Scurr – *Advanced Materials and Healthcare Technologies, School of Pharmacy, University of Nottingham, Nottingham NG7 2RD, U.K.;* orcid.org/0000-0003-0859-3886

Luis Lanzetta – *Institute of Advanced Materials (INAM), Universitat Jaume I, Castelló 12006, Spain;* orcid.org/0000-0001-5591-1010

Francisco Fabregat-Santiago – *Institute of Advanced Materials (INAM), Universitat Jaume I, Castelló 12006, Spain;* orcid.org/0000-0002-7503-1245

Iván Mora-Seró – *Institute of Advanced Materials (INAM), Universitat Jaume I, Castelló 12006, Spain;* orcid.org/0000-0003-2508-0994

Complete contact information is available at: https://pubs.acs.org/doi/10.1021/acsenergylett.6c01829

Author contributions

R.S.S. conceived the original idea, designed the PeLED, QLED, and OLED architectures (including custom sample holders for reliable characterization), engineered the customized VMEL measurement setup (software and hardware), designed the experimental protocols, acquired and analyzed the majority of the data, led the physical interpretation of the comprehensive dataset, wrote the original draft of the manuscript, and supervised the overall project. A.V.-A. synthesized the PeNCs,

https://doi.org/10.1021/acsenergylett.6c01829
ACS Energy Lett. XXXX, XXX, XXX–XXX

fabricated the devices, and acquired the $J-V$, $L-V$, CE$-J$, and EQE$-J$ characteristics of the PeLEDs. S.K. fabricated the devices for the ToF-SIMS studies. A.M.K., M.P., and D.J.S. acquired and analyzed the ToF-SIMS data. L.L. contributed to the scientific discussion and the review of the manuscript. F.F.-S. contributed to the scientific interpretation of IS and VMEL data and the review of the manuscript. I.M.-S. contributed to the interpretation of the data and the review of the manuscript.

Notes

The authors declare no competing financial interest.

■ ACKNOWLEDGMENTS

This work was partially funded by the Ministerio de Ciencia e Innovación of the Spanish Government by the project PLEDs, PID2022-140090OB-C21/AEI/10.13039/501100011033/FEDER. F.F.-S. acknowledges project PID2023-149158OB-C41 (ADD) funded by MICIU/AEI/10.13039/501100011033 and by ERDF A way of making Europe.

■ REFERENCES

(1) Shamsi, J.; Urban, A. S.; Imran, M.; Trizio, L. D.; Manna, L. Metal Halide Perovskite Nanocrystals: Synthesis, Post-Synthesis Modifications, and Their Optical Properties. *Chem. Rev.* **2019**, *119* (5), 3296−3348.

(2) Gualdron-Reyes, A. F.; Masi, S.; Mora-Sero, I. Progress in Halide-Perovskite Nanocrystals with near-Unity Photoluminescence Quantum Yield. *Trends Chem.* **2021**, *3* (6), 499−511.

(3) Su, R.; Xu, Z.; Wu, J.; Luo, D.; Hu, Q.; Yang, W.; Yang, X.; Zhang, R.; Yu, H.; Russell, T. P. Dielectric Screening in Perovskite Photovoltaics. *Nat. Commun.* **2021**, *12* (1), 2479.

(4) Miyata, A.; Mitioglu, A.; Plochocka, P.; Portugall, O.; Wang, J. T.-W.; Stranks, S. D.; Snaith, H. J.; Nicholas, R. J. Direct Measurement of the Exciton Binding Energy and Effective Masses for Charge Carriers in Organic−Inorganic Tri-Halide Perovskites. *Nat. Phys.* **2015**, *11* (7), 582−587.

(5) Kim, J. S.; Heo, J.-M.; Park, G.-S.; Woo, S.-J.; Cho, C.; Yun, H. J.; Kim, D.-H.; Park, J.; Lee, S.-C.; Park, S.-H.; Yoon, E.; Greenham, N. C.; Lee, T.-W. Ultra-Bright, Efficient and Stable Perovskite Light-Emitting Diodes. *Nature* **2022**, *611* (7937), 688−694.

(6) Jiang, M.; Zhang, X.; Wang, F. Efficient Perovskite Nanograin Light-Emitting Diodes in Green-to-Blue Gamut with Co-Additive Engineering. *Adv. Mater.* **2024**, *36* (29), 2400565.

(7) Ding, S.; Wang, Q.; Gu, W.; Tang, Z.; Zhang, B.; Wu, C.; Zhang, X.; Chen, H.; Zhang, X.; Cao, R. Phase Dimensions Resolving of Efficient and Stable Perovskite Light-Emitting Diodes at High Brightness. *Nat. Photonics* **2024**, *18* (4), 363−370.

(8) Kim, Y.-H.; Kim, S.; Kakekhani, A.; Park, J.; Park, J.; Lee, Y.-H.; Xu, H.; Nagane, S.; Wexler, R. B.; Kim, D.-H. Comprehensive Defect Suppression in Perovskite Nanocrystals for High-Efficiency Light-Emitting Diodes. *Nat. Photonics* **2021**, *15* (2), 148−155.

(9) Cho, H.; Jeong, S.-H.; Park, M.-H.; Kim, Y.-H.; Wolf, C.; Lee, C.-L.; Heo, J. H.; Sadhanala, A.; Myoung, N.; Yoo, S. Overcoming the Electroluminescence Efficiency Limitations of Perovskite Light-Emitting Diodes. *Science* **2015**, *350* (6265), 1222−1225.

(10) Dey, A.; Ye, J.; De, A.; Debroye, E.; Ha, S. K.; Bladt, E.; Kshirsagar, A. S.; Wang, Z.; Yin, J.; Wang, Y.; Quan, L. N.; Yan, F.; Gao, M.; Li, X.; Shamsi, J.; Debnath, T.; Cao, M.; Scheel, M. A.; Kumar, S.; Steele, J. A.; Gerhard, M.; Chouhan, L.; Xu, K.; Wu, X.; Li, Y.; Zhang, Y.; Dutta, A.; Han, C.; Vincon, I.; Rogach, A. L.; Nag, A.; Samanta, A.; Korgel, B. A.; Shih, C.-J.; Gamelin, D. R.; Son, D. H.; Zeng, H.; Zhong, H.; Sun, H.; Demir, H. V.; Scheblykin, I. G.; Mora-Seró, I.; Stolarczyk, J. K.; Zhang, J. Z.; Feldmann, J.; Hofkens, J.; Luther, J. M.; Pérez-Prieto, J.; Li, L.; Manna, L.; Bodnarchuk, M. I.; Kovalenko, M. V.; Roeffaers, M. B. J.; Pradhan, N.; Mohammed, O. F.; Bakr, O. M.; Yang, P.; Müller-Buschbaum, P.; Kamat, P. V.; Bao, Q.; Zhang, Q.; Krahne, R.; Galian, R. E.; Stranks, S. D.; Bals, S.; Biju, V.; Tisdale, W. A.; Yan, Y.; Hoye, R. L. Z.; Polavarapu, L. State of the Art and Prospects for Halide Perovskite Nanocrystals. *ACS Nano* **2021**, *15* (7), 10775−10981.

(11) Hassan, Y.; Park, J. H.; Crawford, M. L.; Sadhanala, A.; Lee, J.; Sadighian, J. C.; Mosconi, E.; Shivanna, R.; Radicchi, E.; Jeong, M.; Yang, C.; Choi, H.; Park, S. H.; Song, M. H.; De Angelis, F.; Wong, C. Y.; Friend, R. H.; Lee, B. R.; Snaith, H. J. Ligand-Engineered Bandgap Stability in Mixed-Halide Perovskite LEDs. *Nature* **2021**, *591* (7848), 72−77.

(12) Almeida da Silva, T. C.; Sánchez, R. S.; Alberola-Borràs, J.; Vidal, R.; Mora-Seró, I.; Julián-López, B. Advancing Scalability and Sustainability of Perovskite Light-Emitting Diodes Through the Microwave Synthesis of Nanocrystals. *Energy Environ. Mater.* **2025**, *8* (1), e12810.

(13) Kim, D.-H.; Woo, S.-J.; Huelmo, C. P.; Park, M.-H.; Schankler, A. M.; Dai, Z.; Heo, J.-M.; Kim, S.; Reuveni, G.; Kang, S. Surface-Binding Molecular Multipods Strengthen the Halide Perovskite Lattice and Boost Luminescence. *Nat. Commun.* **2024**, *15* (1), 6245.

(14) Jang, K. Y.; Chang, S. E.; Kim, D.; Yoon, E.; Lee, T. Nanocrystalline Perovskites for Bright and Efficient Light-Emitting Diodes. *Adv. Mater.* **2025**, *37* (25), 2415648.

(15) Chen, D.; Zou, G.; Wu, Y.; Tang, B.; Rogach, A. L.; Yip, H. Metal Halide Perovskite LEDs for Visible Light Communication and Lasing Applications. *Adv. Mater.* **2025**, *37* (25), 2414745.

(16) Han, T.-H.; Jang, K. Y.; Dong, Y.; Friend, R. H.; Sargent, E. H.; Lee, T.-W. A Roadmap for the Commercialization of Perovskite Light Emitters. *Nat. Rev. Mater.* **2022**, *7* (10), 757−777.

(17) Cho, H.; Kim, Y.-H.; Wolf, C.; Lee, H.-D.; Lee, T.-W. Improving the Stability of Metal Halide Perovskite Materials and Light-Emitting Diodes. *Adv. Mater.* **2018**, *30* (42), 1704587.

(18) Calvin, J. J.; Brewer, A. S.; Alivisatos, A. P. The Role of Organic Ligand Shell Structures in Colloidal Nanocrystal Synthesis. *Nat. Synth.* **2022**, *1* (2), 127−137.

(19) Singh, S.; Sen, A.; Aneesha, S. L.; Jeong, W. H.; Ghorai, A.; Ye, J.; Okamoto, T.; Gaur, D.; Samanta, S.; Wang, C.-Y.; Gómez-Graña, S.; Saliba, M.; Govind Rao, V.; Sen, P.; Hoye, R. L. Z.; Biju, V.; Polavarapu, L. Defect Passivation Strategies in Halide Perovskite Solar Cells and LEDs. *ACS Energy Lett.* **2026**, *11* (4), 3060−3120.

(20) Kazes, M.; Udayabhaskararao, T.; Dey, S.; Oron, D. Effect of Surface Ligands in Perovskite Nanocrystals: Extending in and Reaching Out. *Acc. Chem. Res.* **2021**, *54* (6), 1409−1418.

(21) Morad, V.; Stelmakh, A.; Svyrydenko, M.; Feld, L. G.; Boehme, S. C.; Aebli, M.; Affolter, J.; Kaul, C. J.; Schrenker, N. J.; Bals, S.; Sahin, Y.; Dirin, D. N.; Cherniukh, I.; Raino, G.; Baumketner, A.; Kovalenko, M. V. Designer Phospholipid Capping Ligands for Soft Metal Halide Nanocrystals. *Nature* **2024**, *626* (7999), 542−548.

(22) Mirabelli, A. J.; Kammlander, B.; Lu, Y.; Varma, R. M.; Gu, Q.; Radetzky, K.; Selby, T. A.; Liu, T.; Riva, S.; Wei, Z.; Lee, T.-L.; Rawle, J.; Rensmo, H.; Anaya, M.; Cappel, U. B.; Stranks, S. D. Interfacial Chemistry Limits the Stability of Deep Blue Perovskite LEDs Revealed by Operando Characterization. *ACS Energy Lett.* **2025**, *10* (7), 3533−3543.

(23) Singh, S.; Behera, T.; Chowdhury, A. Ion Migration Engenders Synchronous Localized Electroluminescence Blinking in Halide Perovskite Single-Crystal LEDs. *ACS Energy Lett.* **2026**, *11* (6), 4410−4419.

(24) Sánchez, R. S.; Villanueva-Antolí, A.; Bou, A.; Ruiz-Murillo, M.; Mora-Seró, I.; Bisquert, J. Radiative Recombination Processes in Halide Perovskites Observed by Light Emission Voltage Modulated Spectroscopy. *Adv. Mater.* **2023**, *35* (11), 2207993.

(25) Filipoiu, N.; Preda, A. T.; Anghel, D.-V.; Patru, R.; Brophy, R. E.; Kateb, M.; Besleaga, C.; Tomulescu, A. G.; Pintilie, I.; Manolescu, A.

Capacitive and Inductive Effects in Perovskite Solar Cells: The Different Roles of Ionic Current and Ionic Charge Accumulation. *Phys. Rev. Appl.* **2022**, *18* (6), 064087.
(26) Bennett, L. J.; Riquelme, A. J.; Anta, J. A.; Courtier, N. E.; Richardson, G. Avoiding Ionic Interference in Computing the Ideality Factor for Perovskite Solar Cells and Analytical Theory of Their Impedance-Spectroscopy Response. *Phys. Rev. Appl.* **2023**, *19* (1), 014061.
(27) Riquelme, A. J.; Valadez-Villalobos, K.; Boix, P. P.; Oskam, G.; Mora-Seró, I.; Anta, J. A. Understanding Equivalent Circuits in Perovskite Solar Cells Insights from Drift-Diffusion Simulation. *Phys. Chem. Chem. Phys.* **2022**, *24* (26), 15657−15671.
(28) Clarke, W.; Richardson, G.; Cameron, P. Understanding the Full Zoo of Perovskite Solar Cell Impedance Spectra with the Standard Drift-Diffusion Model. *Adv. Energy Mater.* **2024**, *14* (32), 2400955.
(29) Mannar, S.; Mandal, P.; Roy, A.; Viswanatha, R. Experimental Determination of the Molar Absorption Coefficient of Cesium Lead Halide Perovskite Quantum Dots. *J. Phys. Chem. Lett.* **2022**, *13* (27), 6290−6297.
(30) Protesescu, L.; Yakunin, S.; Bodnarchuk, M. I.; Krieg, F.; Caputo, R.; Hendon, C. H.; Yang, R. X.; Walsh, A.; Kovalenko, M. V. Nanocrystals of Cesium Lead Halide Perovskites ($CsPbX_3$, X= Cl, Br, and I): Novel Optoelectronic Materials Showing Bright Emission with Wide Color Gamut. *Nano Lett.* **2015**, *15* (6), 3692−3696.
(31) Nedelcu, G.; Protesescu, L.; Yakunin, S.; Bodnarchuk, M. I.; Grotevent, M. J.; Kovalenko, M. V. Fast Anion-Exchange in Highly Luminescent Nanocrystals of Cesium Lead Halide Perovskites ($CsPbX_3$, X= Cl, Br, I). *Nano Lett.* **2015**, *15* (8), 5635−5640.
(32) Koscher, B. A.; Bronstein, N. D.; Olshansky, J. H.; Bekenstein, Y.; Alivisatos, A. P. Surface-vs Diffusion-Limited Mechanisms of Anion Exchange in $CsPbBr_3$ Nanocrystal Cubes Revealed through Kinetic Studies. *J. Am. Chem. Soc.* **2016**, *138* (37), 12065−12068.
(33) Scharf, E.; Krieg, F.; Elimelech, O.; Oded, M.; Levi, A.; Dirin, D. N.; Kovalenko, M. V.; Banin, U. Ligands Mediate Anion Exchange between Colloidal Lead-Halide Perovskite Nanocrystals. *Nano Lett.* **2022**, *22* (11), 4340−4346.
(34) Mizusaki, J.; Arai, K.; Fueki, K. Ionic Conduction of the Perovskite-Type Halides. *Solid State Ion.* **1983**, *11* (3), 203−211.
(35) McGovern, L.; Futscher, M. H.; Muscarella, L. A.; Ehrler, B. Understanding the Stability of MAPbBr3 versus MAPbI3: Suppression of Methylammonium Migration and Reduction of Halide Migration. *J. Phys. Chem. Lett.* **2020**, *11* (17), 7127−7132.
(36) Fonseca, A. F. V.; Scalon, L.; Vale, B. R. C.; Guaita, M. G. D.; Bettini, J.; Brandão, Z. C.; Zagonel, L. F.; Padilha, L. A.; Nogueira, A. F. In Situ PL Tracking of Halide Exchange at 3D/QD Heterojunction Perovskite Solar Cells. *ACS Energy Lett.* **2024**, *9* (6), 3177−3186.
(37) Zhang, H.; Fu, X.; Tang, Y.; Wang, H.; Zhang, C.; Yu, W. W.; Wang, X.; Zhang, Y.; Xiao, M. Phase Segregation Due to Ion Migration in All-Inorganic Mixed-Halide Perovskite Nanocrystals. *Nat. Commun.* **2019**, *10* (1), 1088.
(38) Wuttig, M.; Schön, C.; Schumacher, M.; Robertson, J.; Golub, P.; Bousquet, E.; Gatti, C.; Raty, J. Halide Perovskites: Advanced Photovoltaic Materials Empowered by a Unique Bonding Mechanism. *Adv. Funct. Mater.* **2022**, *32* (2), 2110166.
(39) Eames, C.; Frost, J. M.; Barnes, P. R. F.; O'regan, B. C.; Walsh, A.; Islam, M. S. Ionic Transport in Hybrid Lead Iodide Perovskite Solar Cells. *Nat. Commun.* **2015**, *6* (1), 7497.

https://doi.org/10.1021/acsenergylett.6c01829
ACS Energy Lett. XXXX, XXX, XXX−XXX